

1 **Emergence of Climate Change in the Tropical Pacific**

2 Jun Ying^{1,2,3*}, Matthew Collins³, Wenju Cai^{4,5,6}, Axel Timmermann^{7,8}, Ping Huang^{9,10},
3 Dake Chen^{1,2,11}, and Karl Stein^{7,8}

4 1. *State Key Laboratory of Satellite Ocean Environment Dynamics, Second Institute*
5 *of Oceanography, Ministry of Natural Resources, Hangzhou, China*

6 2. *Southern Marine Science and Engineering Guangdong Laboratory (Zhuhai),*
7 *Zhuhai, China*

8 3. *College of Engineering, Mathematics and Physical Sciences, University of Exeter,*
9 *Exeter, United Kingdom*

10 4. *Frontier Science Centre for Deep Ocean Multispheres and Earth System and*
11 *Physical Oceanography Laboratory, Ocean University of China, Qingdao, China.*

12 5. *Qingdao National Laboratory for Marine Science and Technology, Qingdao, China.*

13 6. *Centre for Southern Hemisphere Oceans Research (CSHOR), CSIRO Oceans and*
14 *Atmosphere, Hobart, TAS, Australia.*

15 7. *Center for Climate Physics, Institute for Basic Science (IBS), Busan, South Korea.*

16 8. *Pusan National University, Busan, South Korea.*

17 9. *Center for Monsoon System Research, Institute of Atmospheric Physics, Chinese*
18 *Academy of Sciences, Beijing, China*

19 10. *State Key Laboratory of Numerical Modeling for Atmospheric Sciences and*

20 *Geophysical Fluid Dynamics, Institute of Atmospheric Physics, Chinese Academy*
21 *of Sciences, Beijing, China*

22 *11. School of Oceanography, Shanghai Jiao Tong University, Shanghai, China*

23 *Corresponding to: yingjun@sio.org.cn

24

Abstract

Future changes in both the mean climate of the tropical Pacific and the characteristics of the El Niño–Southern Oscillation (ENSO) are now established as being likely. Determining the time of emergence (ToE) of detectable climate change signals against the background noise of natural variability is critical to mitigation strategies and adaptation planning. Here, **using climate model simulations**, we find that the annual-mean **sea surface temperature** (SST) signal, mainly reflecting the tropical-mean warming, has already emerged in the historical period across much of the tropical Pacific, **but appear** last in the east. The annual-mean rainfall signal of a wetter eastern tropical Pacific is expected to emerge by around mid-century based on the multi-model ensemble mean (MEM) result, with some sensitivity to emission scenario. By contrast, the signal of ENSO-related rainfall variability is projected to emerge by around 2040 based on the MEM regardless of emission scenario, ~ 30 years **earlier** than that of ENSO-related SST variability **at ~ 2070** . Our results are instructive for the detection of climate change signals in the tropical Pacific and reinforce the severe risks of ENSO-induced climate extremes that are fast emerging regardless of any mitigation actions.

Main Text:

Hosting the El Niño–Southern Oscillation (ENSO), the world’s largest source of interannual variability, the tropical Pacific plays a pivotal role in human-induced global climate change¹. How the tropical Pacific responds to rising anthropogenic greenhouse gases (GHGs) has been one of the most important issues in the climate science^{2–4}. The mean state SST changes projected by coupled general circulation models (CGCMs) display, on average, a faster eastern equatorial warming than surrounding regions, characterized by a weakened west-minus-east SST gradient^{5,6}. However, recent observations show an enhanced west-minus-east SST gradient and an eastern equatorial cooling, although the pattern of change is sensitive to the SST reconstruction used and the period over which the trend is calculated^{7,8}. The tropical Pacific rainfall generally increases in regions where there is more SST warming than the tropical-mean—the so-called “warmer gets wetter” paradigm^{4,9}, which is accompanied by an eastward shift of the Pacific Walker circulation¹⁰.

On interannual timescales, ENSO-related SST variability (hereafter ENSO SST) is projected to increase^{11–14}, decrease^{15–17}, or unchanged^{18,19}, indicating a large inter-model diversity^{20–22}. In contrast, the change in ENSO-related rainfall variability (hereafter ENSO rainfall) is projected to increase with a robust inter-model consensus^{23–25}, owing to increased mean-state moisture and faster warming in the eastern equatorial Pacific (EEP).

However, it remains unclear when and how these anthropogenic signals will emerge out of the large background noise of natural variability, and few studies have addressed the potential detectability of human-induced ENSO variance changes^{13,26,27}. This knowledge is fundamental for adaptation planning and risk assessment for affected

regions¹³, which is also physically connected with other detectable signals such as the Pacific Walker circulation²⁸⁻³⁰ and sea level³¹⁻³³. Here we use outputs of climate models participating in Coupled Model Intercomparison Project Phase 6 (CMIP6) (ref. ³⁴) to determine the time of emergence (ToE) of the anthropogenic climate change signal in the tropical Pacific relative to the background noise in terms of tropical mean state²¹ and ENSO variability.

Time of Emergence of Mean SST and Rainfall Change Signals

We begin by investigating the ToE of annual-mean SST based on 23 CMIP6 models under historical forcing before 2014 and various shared socio-economic pathway (SSP) emission scenarios thereafter. This requires estimates of both signal and noise of annual-mean SST (see “Signal, noise, and ToE of *annual-mean* SST and rainfall” in Methods). A map of the multi-model ensemble mean (MEM) regression coefficients, representing the response of annual-mean SST to global warming, displays a basin-wide warming in the tropical Pacific together with more warming in the EEP³⁵ (Fig. 1a, shaded), consistent with previous studies based on CMIP3 (ref. ³⁶) and CMIP5 (ref. ⁵) models. The spatial pattern of the noise exhibits largest values in the EEP region due to ENSO variability⁶ (Fig. 1a, Contours). The spatial pattern of the ToE of annual-mean SST indicates that the climate change signal should already be detectable across almost the whole tropical Pacific, with the signal emerging last in the EEP where the noise is the largest (Fig. 1b; Supplementary Fig. 1). The distribution of the ToE and the noise have a similar pattern, with the spatial correlation of up to 0.8 in the MEM (Fig. 1b) and being statistically significant in all individual models (Supplementary Fig. 1), indicating a dominant role of the noise in shaping the spatial distribution of the ToE of annual-mean SST in models.

On the other hand, the MEM annual-mean rainfall response to global warming displays a robust increase along the central to eastern equatorial Pacific with a high inter-model consensus, which is linked to the consistent eastward migration of the Pacific Walker circulation¹⁰, and there is less inter-model consistency on the flanks of the climatological Intertropical Convergence Zone (ITCZ) and South Pacific Convergence Zone (SPCZ) (Fig. 1c, shaded), in agreement with previous studies^{9,37}. The MEM noise of annual-mean rainfall exhibits a pattern with large values in the central equatorial Pacific, ITCZ and SPCZ regions, and relatively small values in the EEP (Fig. 1c, contours). The estimated MEM ToE in most models under the SSP585 scenario, indicates that the annual-mean rainfall signal can be expected to emerge within the coming decades in the EEP, although no emergent signal appears in the ITCZ and the SPCZ by the end of the 21st century (Fig. 1d).

We then focus on the EEP region where both detectable signals of annual-mean SST and rainfall emerge in the 21st century in most models (Fig. 1b, d). As shown in Fig. 2a, the MEM annual-mean SST signals emerge at around 2015 under all four emission scenarios, earlier than the ToE in the three sets of SST observations, in which signals are undetectable by 2019. For individual models under the SSP585 scenario, 12 out of 23 models already have detectable annual-mean SST signals in the EEP before 2020, with signals emerging as early as the late 1990s (Fig. 2b). The spatial patterns of the ToE of observed annual-mean SST show the signal emerging in most parts of the tropical Pacific by 2019 but not in the EEP (Supplementary Fig. 2).

Given that the background noise between MEM results and observations are comparable in magnitude (Fig. 2c), the model-observation discrepancy in the ToE of EEP annual-mean SST change is attributable to different signals (Extended Data Fig. 1a). Differences in signals of annual-mean SST can be further traced back to different

responses of local annual-mean SST to global warming (bottom row in Fig. 2d), as the model-observation discrepancy in the global-mean SST change is negligible (Extended Data Fig. 1b–c). The responses of observed annual-mean SST, though with a similar basin-wide warming, display a pattern with an enhanced west-minus-east SST gradient featuring an EEP minimum warming (Extended Data Fig. 2a–c), in contrast to the local maximum warming in the MEM with a small inter-model difference (Fig. 1a and bottom row in Fig. 2d).

To highlight the spatial variation of SST response to global warming, we further decompose the annual-mean SST into two components: the tropical-mean SST (T_{tm}) and the relative SST (T_r) that is the deviation from the tropical-mean⁴. By doing so, we find the model-observation discrepancy in the EEP annual-mean SST response to global warming is caused by the difference in the response of local T_r , rather than that of T_{tm} (top and middle rows in Fig. 2d). In the MEM, as well as individual models, the T_r shows a robust warming response in the EEP, whereas in observations there is consistent cooling response, albeit with different magnitudes (Fig. 2d and Extended Data Fig. 2d–g).

An inter-model relationship reveals that the ToE of the EEP annual-mean SST is highly correlated to the earlier ToE (earlier than 2000 in all but one of the models) of the T_{tm} ($r=0.88$, Fig. 2e), but not to the much later ToE (later than 2050 in all models) of the EEP T_r (Fig. 2f). Thus, the modelled emergent signals of the EEP annual-mean SST mainly reflect signals of the T_{tm} . The earlier ToE of the T_{tm} is a result of both a stronger response of the T_{tm} (Fig. 2d) and weaker background noise (Supplementary Fig. 3a), while the later ToE of the T_r is caused by both a weaker response of the T_r

(Fig. 2d) and stronger background noise (Supplementary Fig. 3b).

Given comparable ToE of T_{lm} (Fig. 2e) and noise of T_r (Supplementary Fig. 3b) between the MEM results and observations, the model-observation discrepancy in the ToE of annual-mean SST is thus mainly due to the widely-discussed difference between a warming response of T_r in the EEP, featuring a weakened west-minus-east SST gradient in models and an opposite response in observations. Although the cause for such opposing responses is still a matter of debate³⁸⁻⁴², we find that both the modelled and observed responses of EEP T_r are dependent on the length of the time period over which the responses are computed. Regardless of whether the modelled EEP T_r response is warming or cooling in the relatively short historical simulations, it can be warming in future projections when the time period is extended to the end of 21st century (Extended Data Fig. 3). Thus, we cannot exclude the possibility that a pattern with an EEP warming response of T_r featuring a weakened west-minus-east SST gradient will emerge in the future as GHGs forcing continues.

For rainfall in the EEP, we focus on the model outputs, as observational records are reliable only during the satellite era, thus are too short to capture the long-term global warming-induced signal⁴³. The estimated MEM ToE under different emission scenarios shows that detectable signals of annual-mean rainfall can be found around mid-century under the SSP245, SSP370 and SSP585 scenarios (in years 2070, 2054 and 2043, respectively), but not under the SSP126 scenario which features the lowest GHGs forcing (Fig. 3a). For individual models under the most aggressive SSP585 scenario, all models but two show detectable signals of annual-mean rainfall by the end of 21st century, while all models but two do not show detectable signals before 2020 (Fig. 3b), suggesting a robust inter-model consensus of the undetectability of an annual-

mean rainfall signal by now. The inter-model difference in the ToE of annual-mean rainfall, with signals emerging as early as before 2020 in a few models (such as CanESM5) and as late as after 2080 in other models (such as MPI-ESM1-2-LR), is larger than that of annual-mean SST. Nevertheless, the estimated ToE of EEP annual-mean rainfall is later than that of annual-mean SST in all models by several decades (Fig. 2b, 3b).

To investigate the cause of a later ToE of annual-mean rainfall, we decompose rainfall change into a thermodynamic component ($-\bar{\omega} \cdot \Delta q$) due to moisture change, and a dynamic component ($-\Delta \omega \cdot \bar{q}$) due to circulation change based on a simplified moisture budget analysis³⁷. The result indicates that the weak response of annual-mean rainfall in the ITCZ and SPCZ is caused by an offsetting effect between a positive response of the thermodynamic component and a negative response of the dynamic component, while the robust positive response of EEP annual-mean rainfall is almost entirely due to the dynamic component—an equatorial and eastward shift in rainfall (Supplementary Fig. 4), in agreement with previous studies^{24,25}. As such, the ToE of EEP annual-mean rainfall appears to not be influenced by the thermodynamic component (Fig. 3c, d). Rather, it is almost totally determined by the ToE of dynamic component, with the inter-model correlation coefficient between the two being up to 0.97 (Fig. 3e).

The response of the EEP $-\Delta \omega \cdot \bar{q}$ is controlled by an ascending circulation response, which is driven by a local positive warming response of T_r (Supplementary Fig. 4b, contours), suggestive of the “warmer gets wetter” paradigm^{4,37}. The significant inter-model relationship between the response of $-\Delta \omega \cdot \bar{q}$ and T_r and the insignificant relationship with T_{tm} in the EEP (Extended Data Fig. 4) further confirms

that it is the T_r , rather than the T_{tm} , that plays an important role in the response of $EEP - \Delta\omega \cdot \bar{q}$. This contributes to a later ToE of annual-mean rainfall compared with that of the annual-mean SST, which mainly reflects the early ToE of the tropical-mean SST (Fig. 2e). Likewise, we would expect the signal of observed annual-mean rainfall to emerge later than the signal of observed annual-mean SST.

Time of Emergence of ENSO SST and Rainfall Change Signals

ENSO dominates interannual climate variability in the tropical Pacific, displaying anomalous SST and rainfall over the central to eastern equatorial Pacific^{44,45}. The CMIP6 MEM results for the reference pattern over 1960 to 1989, capture the common features of ENSO (Fig. 4a, b), although there are common biases such as an excessive westward extension of ENSO SST and rainfall^{46,47}. The map of MEM regression coefficients under the four SSP scenarios, representing the response of ENSO SST to global warming (see “Signal, noise and ToE of ENSO SST and rainfall” in Methods), all display an enhancement in SST variability, as well as a westward-shift relative to the reference pattern, with a robust inter-model agreement (Fig. 4c and Extended Data Fig. 5a–c). The modelled enhanced ENSO SST response is consistent with the observations, although the westward-shifts are hard to detect in the limited historical period in observations (Extended Data Fig. 5d–f). The MEM response of ENSO rainfall, on the other hand, displays a consistent enhancement and an eastward-shift relative to the reference pattern^{23,24} (Fig. 4d and Extended Data Fig. 5g–i).

To capture the commonality of the spatial distribution of ENSO ToE for most models, the MEM results of ENSO SST and rainfall ToE are shown by averaging model results only when more than 70% of models have local emergent signals before the last 30-year time window of 21st century (Fig. 4e, f). The results indicate that both emergent

signals of ENSO SST and rainfall change are confined to the equatorial region and are not detectable **by now**. The MEM ToE of the ENSO SST signal is located to the west of the referenced ENSO SST center (Fig. 4e), while the MEM ToE of the ENSO rainfall signal is located to the east of the referenced ENSO rainfall center (Fig. 4f). Thus, besides the increased amplitude responses to global warming, the pattern shifts of both ENSO SST and rainfall **contribute to** their respective times of emergence.

To confirm, we decompose the response of grid-point ENSO SST and rainfall to global warming into two components: the amplitude response and the structural response. The former depicts the intensity change by assuming that the spatial pattern under global warming is fixed, while the latter indicates shifts in spatial pattern (see “**Separation of amplitude and structural changes in ENSO SST and rainfall**” in **Methods**). For ENSO SST, **the increased amplitude response plays a greater role than the response of structural change** (Supplementary Fig. 5a, b). **In contrast**, for ENSO rainfall, the eastward-shifted structural response plays a more important role in the ENSO rainfall response compared with the increased amplitude response (Supplementary Fig. 5c, d).

A comparison between the ToE of ENSO SST and rainfall change signals in the EEP reveals that the modelled ToE of ENSO rainfall signal is generally earlier than that of ENSO SST signal by several decades (Fig. 5a–d), which is opposite to the ToE **behavior of the** annual-mean SST and rainfall change signals. In the MEM, the ENSO SST signal is expected to emerge under both the SSP585 and SSP370 scenarios in the 30-year time windows ending at 2070 and 2073, respectively, but not under the other two lower scenarios (SSP126 and SSP245) (Fig. 5a), indicative of some sensitivity to emission scenarios. The ToE of ENSO rainfall, however, is projected to be in this century under all the SSP126, SSP245, SSP370 and SSP585 scenarios in the 30-year

time windows ending at 2039, 2045, 2042 and 2037, respectively, separated by less than a decade (Fig. 5b). Under SSP585 and SSP370 scenarios, ToE of ENSO rainfall is ~ 30 years earlier than that of ENSO SST.

As exemplified by the results projected under the SSP585 scenario, the estimated ToE of ENSO rainfall is also earlier than that of ENSO SST in most individual models (Fig. 5c, d and Supplementary Fig. 6). For ENSO SST, 17 out of 23 (around 74%) models show a ToE before the end of the 21st century (Fig. 5c), while for ENSO rainfall, all but one model (INM-CM5-0) shows the signal emerging (Fig. 5d). A large inter-model spread exists in the ToE of both ENSO SST and rainfall, with the inter-model standard deviation up to 50 years (Fig. 5c, d), which, however, does not change our result of an earlier ToE of ENSO rainfall than ENSO SST. Thus, the signal of ENSO-related variability change, when measured by rainfall^{6,24}, is stronger and will emerge earlier as compared to that measured by SST.

To explore the cause of an earlier ToE of ENSO rainfall, we decompose ENSO rainfall change into a thermodynamic component ($-\bar{\omega}' \cdot \Delta q_c$) due to climatological moisture change, and a dynamic component ($-\Delta \omega' \cdot \bar{q}_c$) due to ENSO-driven atmospheric circulation change¹⁵ (see “Decomposition of 30-year climatological SST and ENSO rainfall change” in Methods). The responses of both thermodynamic and dynamic components contribute to the increase in ENSO rainfall in the EEP, with the latter playing the major role (supplementary Fig. 7). Thus, the ToE of ENSO rainfall appears to be dominated by the ToE of dynamic component (Fig. 5e), while the much earlier ToE of thermodynamic component (Fig. 5f), though playing a minor role, hastens the ToE of ENSO rainfall (Extended Data Fig. 6a). The ToE of dynamic component of ENSO rainfall, on the other hand, is controlled by that of the

climatological relative SST change, with an inter-model correlation coefficient between the two reaching up to 0.69 (Fig. 5g), indicating a “warmer gets wetter” paradigm on interannual timescale^{48,49}. As the ToE of climatological relative SST change is earlier than that of ENSO SST (Fig. 5a and Extended Data Fig. 6b), the ToE of ENSO rainfall is also earlier. In addition, the insensitivity of the ToE of ENSO rainfall to emission scenarios is attributable to the climatological relative SST change, which is also insensitive to emission scenarios (Extended Data Fig. 6b).

Implications for Emergence of Rainfall Signals

Our estimations for ToE of annual-mean rainfall in the EEP based on MEM reveal that they are dependent on the future emission scenarios, with signals emerging as early as before 2050 under the SSP585 scenario; by contrast, annual-mean rainfall is undetectable by the end of this century under the lowest SSP126 scenario (Fig. 3a). This implies that climate mitigation could be effective in preventing significant rainfall shifts in the mean state. However, the estimated MEM ToE of ENSO rainfall are only a few years apart in the different emission scenarios (Fig. 5b). Hence, we would expect to detect a significant signal of ENSO rainfall change before 2050 even if we follow a strong mitigation pathway such as the SSP126 or SSP245 scenarios. Considering that ENSO rainfall is the main driver of global ENSO teleconnections, via heating of the atmosphere and the propagation of atmospheric waves to both the tropics and extratropics⁵⁰, the emergent ENSO rainfall change signal could trigger wide-ranging impacts on natural and human systems.

Summary and Caveats

Our results indicate that the annual-mean SST signal emerges earlier than the annual-mean rainfall, whereas the ENSO-related rainfall signal emerges earlier than the

285 ENSO-related SST **signal**, are robust in most individual models as well as in their
286 aggregation. We note that the estimated ToE could be affected by model biases. **For**
287 **example, the difference between the observed enhancement and a modelled weakening**
288 **in the equatorial Pacific west-minus-east SST gradient likely affects the ToE of annual-**
289 **mean SST (Fig. 2b, d).** However, as we have shown, **the possibility that** a pattern with
290 a weakened west-minus-east SST gradient should not be excluded in the future real
291 world, **given that all models generate SST warming in the EEP in the future with more**
292 **GHGs forcing regardless of their behaviors in the historical simulations.** The second
293 **source of uncertainty is a large inter-model difference in the exact ToE, owing to**
294 **differences either in the background noise of natural variability, the climate change**
295 **signals in response to global warming, or both.** Thirdly, the estimated ToE in a specific
296 **model could be different in different ensemble member runs with different initial**
297 **conditions in which decadal to multi-decadal internal variability such as the**
298 **interdecadal Pacific oscillation^{8,51,52} is different.** However, the MEM results, which are
299 **the basis of our conclusions, are robust and insensitive to choosing different ensemble**
300 **members.**

301 Despite these caveats, our result of an earlier ToE of annual-mean SST than annual
302 mean rainfall suggests that focus should be placed on the tropical mean SST for
303 detection of mean state change in the tropical Pacific. In addition, our result of a ToE
304 of ENSO rainfall, ~30 years earlier than ENSO SST and insensitive to different
305 emission scenarios, highlights the potential risks of extreme events associated with
306 ENSO rainfall change and the associated ENSO teleconnections.

Methods

CMIP6 models, observed datasets, and processing. We use the historical runs for the period 1870–2014, the four tier-one SSP (SSP126, SSP245, SSP370 and SSP585) scenario runs for the period 2015–2099, and the pre-industrial control (piControl) run for the last 500 years from 23 CMIP6 models³⁴. They are ACCESS-CM2, ACCESS-ESM1-5, BCC-CSM2-MR, CanESM5, CESM2-WACCM, CNRM-CM6-1-HR, CNRM-CM6-1, CNRM-ESM2-1, EC-Earth3-Veg, FGOALS-f3-L, FGOALS-g3, GFDL-ESM4, GISS-E2-1-G, INM-CM4-8, INM-CM5-0, IPSL-CM6A-LR, MIROC-ES2L, MIROC6, MPI-ESM1-2-HR, MPI-ESM1-2-LR, MRI-ESM2-0, NorESM2-LM, NorESM2-MM. Note that we have only 499 years in model CESM2-WACCM and 300 years in model CNRM-CM6-1-HR in piControl run. For each model, we use one ensemble member run (r1i1p1f1) **but test the sensitivity to using different members (see “Signal, noise and ToE of ENSO SST and rainfall” below)**. Monthly outputs are used of surface temperature (*ts*, which is SST for open ocean), rainfall (*pr*), surface air specific humidity (*huss*), and vertical pressure velocity (*wap*) at 500hPa. All the model outputs are bilinear interpolated into a $2.5^\circ \times 2.5^\circ$ grid before analyses.

To investigate ToE of observed SSTs, we use three different observational SST datasets: The Hadley Center Sea Ice and SST version 1.1 (HadISSTv1) (ref. ⁵³), the National Oceanic and Atmospheric Administration Extended Reconstructed SST version 5 (ERSSTv5) (ref. ⁵⁴), and the Centennial In Situ Observation-Based Estimates of the Variability of SST and Marine Meteorological Variables version 2 (COBEv2) (ref. ⁵⁵) for the period 1870–2019. **Here we choose the starting year as 1870 in both models and observations to include the global warming signal as much as possible, but note that there are uncertainties in the SST observational datasets due to the sparse data coverage in the early stage of the records⁷. However, our main conclusions hardly change if a**

different starting time between 1870 and 1950 is chosen, since the global warming signals are relatively small before 1950 (Extended Data Fig. 1c).

We take 30 years of the 1960–1989 period as our reference period, as we find good consistency between observational SST datasets in this period. All changes under global warming are calculated by removing the associated values in that reference period. Annual-mean values are calculated simply by averaging the monthly values from January to December. Interannual anomaly fields are obtained by removing the climatological annual cycle of the chosen period and then quadratic de-trending⁵⁶ the monthly values over the chosen period.

Signal, noise, and ToE of *annual-mean* SST and rainfall. To estimate the **signal** of modelled annual-mean SST, we calculate the response of annual-mean SST to global warming. The global warming signal is taken as the annual-mean SST change from the reference period of 1960–1989 averaged over the 60°S–60°N domain and then smoothed by fitting a fourth order polynomial⁵⁷ (Extended Data Fig. 1b, c), written as $\tilde{T}(t)$, $t = 1870 - 2099$. Here we choose the average of SST from 60°S to 60°N to remove inconsistencies caused by sea ice in observational SSTs but not in modelled surface temperature (*ts*). Nevertheless, our conclusions do not change if a different domain, say 90°S–90°N, is chosen to compute the global warming signal. The signal of grid-point annual-mean SST, $S_{\text{AM-SST}}(x, y, t)$, is obtained by regressing grid-point annual-mean SST change onto the smoothed global warming time series $\tilde{T}(t)$:

$$S_{\text{AM-SST}}(x, y, t) = a(x, y) \cdot \tilde{T}(t) + b(x, y) \quad (1),$$

where a is the regression coefficient between $\tilde{T}(t)$ and annual-mean SST,

representing the response of annual-mean SST to global warming (Fig. 1a), and b is the intercept.

The **noise** of grid-point annual-mean SST, $N_{AM-SST}(x, y)$, is defined as the interannual standard deviation of annual-mean SST, which is based on the last 500 years of the piControl run. In observations, calculation of the signal of grid-point annual-mean SST is the same as that in the models except that it is based on the period 1870–2019, while the noise of observational annual-mean SST is obtained by calculating standard deviation of the annual-mean SST after the signal is removed³². Modelled signal ($S_{AM-rainfall}(x, y, t)$) and noise ($N_{AM-rainfall}(x, y)$) of annual-mean rainfall are similarly calculated.

The **ToE** of grid-point annual-mean SST is defined as the year when the grid-point signal-to-noise ratio of annual-mean SST, S_{AM-SST} / N_{AM-SST} , is higher (lower) than 1.0 (–1.0) and all subsequent S_{AM-SST} / N_{AM-SST} stay higher (lower) than 1.0 (–1.0) if the local response of annual-mean SST to global warming ($a(x, y)$) is positive (negative), as in a previous study⁵⁷. Calculation for the modelled ToE of annual-mean rainfall is similar to that for annual-mean SST. The ToE in the EEP is obtained by firstly averaging the signal-to-noise ratio as well as the noise spatially and then calculating it using the method above. Note that the chosen threshold value of S_{AM-SST} / N_{AM-SST} for a detectable annual-mean signal is somewhat subjective. If a larger threshold, say 2.0 (–2.0), is chosen⁵⁷, the estimated times of emergence of annual-mean SST and rainfall would be later by around 20–30 years (not shown), but our result of an earlier ToE of annual-mean SST compared with that of annual-mean rainfall does not change.

Decomposition of *annual-mean* SST and rainfall change. The annual-mean SST change from the reference period in each grid point can be decomposed into a tropical-mean SST (T_{tm}) change averaged over 20°S to 20°N and a relative SST (T_r) that is the deviation from the tropical-mean SST^{4,58}. The annual-mean rainfall change can be decomposed, **from a simplified water vapor budget with the negligible non-linear term removed**, into the changes in thermodynamic and dynamic component^{37,59}:

$$\Delta P(x, y, t) \sim -\Delta \omega(x, y, t) \cdot \overline{q(x, y)} - \overline{\omega(x, y)} \cdot \Delta q(x, y, t) \quad (2),$$

where Δ denotes the change relative to the value in the reference period; the overbar denotes the climatological value in the reference period 1960–1989; q is surface specific humidity and ω is vertical pressure velocity at 500hPa. The term $-\Delta \omega \cdot \bar{q}$ is the dynamic component of annual-mean rainfall change, which represents the contributions of atmospheric circulation change, while the term $-\bar{\omega} \cdot \Delta q$ is the thermodynamic component of annual-mean rainfall change, which represents the contributions of moisture change⁶⁰. **The combination of dynamic and thermodynamic components in equation (2) defines the reconstructed annual-mean rainfall change.**

Signal, noise, and ToE of ENSO SST and rainfall. Empirical orthogonal function (EOF) analysis is used to extract the spatial pattern of ENSO SST in each model and observations in the tropical Pacific (20°S–20°N, 120°E–80°W). For each model, the EOF analysis is performed on interannual anomalies of each 30-year time window moving forward by one year starting from 1870 to 2099, generating an evolution of 30-year running variability for time from 1899 to 2099 (recorded as the ending year of each 30-year time window), $EN_{SST}(x, y, t_e)$, $t_e = 1899 - 2099$, and **an** evolution of change of ENSO SST from the reference period over 1960–1989,

399 $\Delta EN_{SST}(x, y, t_e) = EN_{SST}(x, y, t_e) - \overline{EN_{SST}(x, y)}$. The EOF outputs are arranged such that
 400 the principal components (PCs) are standardized, and the EOF modes describe the
 401 spatial patterns of variability of the modes. The EOF patterns are taken to ensure that
 402 they are in El Niño phase. For simplicity, the first EOF mode in each period defines the
 403 ENSO SST^{15,23}, and ENSO diversity is not considered⁶¹. The ENSO rainfall is defined
 404 by regressing grid-point interannual anomalies of rainfall onto the first PC of ENSO
 405 SST.

406 The evolution of the corresponding global warming signal is taken as the 30-year
 407 climatological SST change from the reference period, smoothed also by fitting a fourth
 408 order polynomial, written as $\tilde{T}_c(t_e)$, corresponding to changes in ENSO SST,
 409 $\Delta EN_{SST}(x, y, t_e)$, in each 30-year time window ending from 1899 to 2099.

410 The evolution of the **signal** of grid-point ENSO SST change, $S_{EN-SST}(x, y, t_e)$, is
 411 obtained by regressing grid-point ENSO SST change $\Delta EN_{SST}(x, y, t_e)$ onto the global
 412 warming time series of $\tilde{T}_c(t_e)$:

$$413 \quad S_{EN-SST}(x, y, t_e) = c(x, y) \cdot \tilde{T}_c(t_e) + d(x, y) \quad (3),$$

414 where $c(x, y)$ is the regression coefficient between $\tilde{T}_c(t_e)$ and $\Delta EN_{SST}(x, y, t_e)$,
 415 representing the response of ENSO SST to global warming (Fig. 4c), and d is the
 416 intercept.

417 To diagnose the **noise** of ENSO SST, the same EOF analysis is applied to each 30-year
 418 time window moving forward by one year for the last 500 years of the piControl run,
 419 which generates 471 realizations of 30-year running grid-point ENSO SST for each
 420 model. Then changes of these realizations from the reference period of 1960–1989 are

defined as the noise, written as $\Delta EN_{SST}(x, y, t_{e-pi})$, where t_{e-pi} represents each of the 30-year time windows in the piControl run. Calculations for the modelled signal of ENSO rainfall ($S_{EN-rainfall}(x, y, t_e)$) and the realizations of ENSO rainfall changes in the piControl run from the reference period ($\Delta EN_{rainfall}(x, y, t_{e-pi})$) are similar to those for ENSO SST.

The **ToE** of ENSO SST is defined as the 30-year time window when the signal, $S_{EN-SST}(x, y, t_e)$, is higher (lower) than the 99% (1%) value of the noise, $\Delta EN_{SST}(x, y, t_{e-pi})$, for grid-point ENSO SST responses to global warming (c in equation (3)) that are positive (negative), and the signals continue to exceed the defined threshold value beyond that time. Note that choosing a different ensemble member run for individual models, say r2i1p1f1, does change the results of estimated ToE of ENSO SST and rainfall for individual models, but our main conclusions do not change, especially considering that they are based on the MEM results. In addition, although the times of emergence of ENSO SST and rainfall do change if a different time window, say a 40-year or 50-year time window, is chosen (the longer the time window, the earlier the ToE of ENSO SST and rainfall), our main conclusion of an earlier ToE of ENSO rainfall than that of ENSO SST also doesn't change.

For observations, calculation of the **signal** of ENSO SST is the same as for models except that it is based on the period 1870–2019. But when calculating the **noise**, we first remove the least squares quadratic trend of the monthly SST value for the whole period 1870–2019, and the remaining is treated as the unforced data, which is analogous to the output in piControl run in models. Then the changes in ENSO SST in each 30-year time window moving forward by one year from the remaining unforced data

relative to the reference period of 1960–1989 are calculated to represent the noise. In an 1870–2019 period, we can obtain 121 samples of such change, which are analogous to the 471 samples of $\Delta EN_{\text{SST}}(x, y, t_{\text{e-pi}})$ in each model. The ToE of observational ENSO SST is estimated by making a comparison between the signal of ENSO SST and the above 121 samples of ENSO SST change in a similar statistical way as in models.

To illustrate, we use one model (EC-Earth3-Veg) and one observational SST (HadISSTv1) and specify a grid-point (0° , 120°W) to give a brief description of how to estimate the ToE of ENSO SST (Supplementary Fig. 8). Both the EC-Earth3-Veg and HadISSTv1 display increased signal of ENSO SST with time for the specified grid-point (Supplementary Fig. 8a), indicating a positive ENSO SST response to global warming. As such, we choose the $\Delta EN_{\text{SST}}(x, y, t_{\text{e-pi}})$ value that is higher than the 99-percentile value of all the variability samples (471 samples for EC-Earth3-Veg and 121 samples for HadISSTv1) as the threshold value for an emergent $S_{\text{EN-SST}}(x, y, t_e)$. The threshold value for EC-Earth3-Veg is 0.3 (horizontal black dashed line in Supplementary Fig. 8), while that for HadISSTv1 is 0.14 (horizontal red dashed line in Supplementary Fig. 8). The ToE of ENSO SST in the specified grid-point is thus defined as the 30-year time window when the $S_{\text{EN-SST}}(x, y, t_e)$ exceeds the threshold value and the signals persist thereafter. As shown in Supplementary Fig. 8a, the ToE of ENSO SST in the specified grid-point for EC-Earth3-Veg is the 30-year time window ending at year 2021, while that for HadISSTv1 does not appear, given that the associated signal does not exceed the corresponding threshold value even in the last 30-year time window (1990–2019).

The calculation for the modelled ToE of ENSO rainfall is similar to that for ENSO SST. The estimated times of emergence of ENSO SST and rainfall could be different when choosing different threshold values for signals, but the main conclusions, such as an earlier ToE of ENSO rainfall than that of ENSO SST and both the ToE of ENSO SST and rainfall are not yet detectable, do not change when other threshold values, for example, the 95% (5%) or 97.5% (2.5%), are chosen (Supplementary Table. 1).

Separation of amplitude and structural changes in ENSO SST and rainfall. The changes in ENSO SST in each 30-year time window from 1870 to 2099 relative to the reference period of 1960–1989, $\Delta EN_{SST}(x, y, t_e)$, are subjected to a “pattern” regression onto ENSO SST pattern in the reference period, $\overline{EN_{SST}(x, y)}$. The linear regression defines the amplitude change in ENSO SST, $\Delta EN_{SST-amp}(x, y, t_e)$:

$$\Delta EN_{SST-amp}(x, y, t_e) = \alpha(t_e) \cdot \overline{EN_{SST}(x, y)} + \beta(t_e) \quad (4),$$

where α is the “pattern” regression coefficient and β is the intercept. And the residual part represents the structural change in ENSO SST, written as $\Delta EN_{SST-str}(x, y, t_e)$:

$$\Delta EN_{SST-str}(x, y, t_e) = \Delta EN_{SST}(x, y, t_e) - \Delta EN_{SST-amp}(x, y, t_e) \quad (5).$$

A separation of ENSO rainfall change is carried out similarly to that of ENSO SST change.

Decomposition of 30-year climatological SST and ENSO rainfall change. As the annual-mean SST change, each of the 30-year climatological-mean SST change from the reference period ending from 1899 to 2099 in each grid point can be decomposed into a tropical-mean climatological SST change averaged over 20°S to 20°N and a

climatological relative SST change that is the deviation from the tropical-mean change. The ENSO rainfall change can be decomposed, from a simplified water vapor budget with negligible terms removed, into the changes in thermodynamic and dynamic component¹⁵:

$$\Delta P'(x, y, t) \sim -\Delta \omega'(x, y, t) \cdot \overline{q_c(x, y)} - \overline{\omega'(x, y)} \cdot \Delta q_c(x, y, t) \quad (6),$$

where Δ denotes the change relative to the value in the reference period; the prime denotes ENSO-related interannual variability; the overbar denotes the climatological value in the reference period 1960–1989; q_c is 30-year climatological surface specific humidity and ω' denotes the ENSO-driven vertical motion variability at 500hPa. The term $-\Delta \omega' \cdot \overline{q_c}$ is the dynamic component of ENSO rainfall change, which represents the contributions of ENSO-driven atmospheric circulation change, while the term $-\overline{\omega'} \cdot \Delta q_c$ is the thermodynamic component of ENSO rainfall change, which represents the contributions of climatological moisture change¹⁵. The combination of dynamic and thermodynamic components in equation (6) defines the reconstructed ENSO rainfall change.

Acknowledgements

J.Y. was supported by the National Natural Science Foundation of China (Grants 41690121, 41690120), the Scientific Research Fund of the Second Institute of Oceanography, Ministry of Natural Resources (Grant QNYC2001), and the Innovation Group Project of the Southern Marine Science and Engineering Guangdong Laboratory (Zhuhai) (No. 311021001). M.C. was supported by a grant from the UK Natural Environment Research Council (NE/S004645/1). W.C. was supported by Centre for Southern Hemisphere Oceans Research, a joint research Center for Southern Hemisphere Oceans Research between QNLM and CSIRO. A.T. and K.S. received funding from the Institute for Basic Science (IBS) under IBS-R028-D1. P.H. was supported by the National Natural Science Foundation of China (Grants 41975116).

516 **Data availability**

517 The CMIP6 model monthly outputs are archived at the Earth System Grid Federation
518 server (<https://esgf-node.llnl.gov/search/cmip5/>). The HadISSTv1 dataset can be
519 obtained from <https://www.metoffice.gov.uk/hadobs/>. The ERSSTv5 and COBEv2
520 datasets are both available from <https://www.esrl.noaa.gov/psd/data/gridded/>.

521

522 **Code availability**

523 All the codes are built on NCAR Command Language (NCL), which can be made
524 available on request.

525

- 527 1 Kosaka, Y. & Xie, S.-P. The tropical Pacific as a key pacemaker of the variable
528 rates of global warming. *Nature Geoscience* **9**, 669-673 (2016).
- 529 2 Knutson, T. R. & Manabe, S. Time-Mean Response over the Tropical Pacific to
530 Increased CO₂ in a Coupled Ocean-Atmosphere Model. *Journal of Climate* **8**, 2181-
531 2199 (1995).
- 532 3 Vecchi, G. A., Clement, A. & Soden, B. J. Examining the Tropical Pacific's
533 Response to Global Warming. *Eos, Transactions American Geophysical Union* **89**, 81-
534 83 (2008).
- 535 4 Xie, S.-P. *et al.* Global Warming Pattern Formation: Sea Surface Temperature and
536 Rainfall. *Journal of Climate* **23**, 966-986 (2010).
- 537 5 Ying, J., Huang, P. & Huang, R. Evaluating the formation mechanisms of the
538 equatorial Pacific SST warming pattern in CMIP5 models. *Advances in Atmospheric*
539 *Sciences* **33**, 433-441 (2016).
- 540 6 Cai, W. *et al.* ENSO and greenhouse warming. *Nature Climate Change* **5**, 849-859
541 (2015).
- 542 7 Deser, C., Phillips, A. S. & Alexander, M. A. Twentieth century tropical sea surface
543 temperature trends revisited. *Geophysical Research Letters* **37** (2010).
- 544 8 Bordbar, M. H., Martin, T., Latif, M. & Park, W. Role of internal variability in
545 recent decadal to multidecadal tropical Pacific climate changes. *Geophysical Research*
546 *Letters* **44**, 4246-4255 (2017).
- 547 9 Widlansky, M. J. *et al.* Changes in South Pacific rainfall bands in a warming
548 climate. *Nature Climate Change* **3**, 417-423 (2013).
- 549 10 Bayr, T., Dommenges, D., Martin, T. & Power, S. B. The eastward shift of the
550 Walker Circulation in response to global warming and its relationship to ENSO
551 variability. *Climate Dynamics* **43**, 2747-2763 (2014).
- 552 11 Cai, W. *et al.* Increased variability of eastern Pacific El Niño under greenhouse
553 warming. *Nature* **564**, 201-206 (2018).
- 554 12 Ying, J., Huang, P., Lian, T. & Chen, D. Intermodel Uncertainty in the Change of
555 ENSO's Amplitude under Global Warming: Role of the Response of Atmospheric
556 Circulation to SST Anomalies. *Journal of Climate* **32**, 369-383 (2019).
- 557 13 Cai, W. *et al.* Changing El Niño–Southern Oscillation in a warming climate. *Nature*
558 *Reviews Earth & Environment* **2**, 628-644 (2021).
- 559 14 Cai, W. *et al.* ENSO Response to Greenhouse Forcing, in *El Niño Southern*
560 *Oscillation in a Changing Climate* (eds McPhaden, M. J., Santoso, A. & Cai, W.) (AGU,
561 2020).
- 562 15 Huang, P. & Xie, S.-P. Mechanisms of change in ENSO-induced tropical Pacific
563 rainfall variability in a warming climate. *Nature Geoscience* **8**, 922-926 (2015).
- 564 16 Callahan, C. W. *et al.* Robust decrease in El Niño/Southern Oscillation amplitude
565 under long-term warming. *Nature Climate Change* **11**, 752-757 (2021).
- 566 17 Wengel, C. *et al.* Future high-resolution El Niño/Southern Oscillation dynamics.
567 *Nature Climate Change* **11**, 758-765 (2021).
- 568 18 Philip, S. & van Oldenborgh, G. J. Shifts in ENSO coupling processes under global

- warming. *Geophysical Research Letters* **33**, L11704 (2006).
- 19 Stevenson, S. L. Significant changes to ENSO strength and impacts in the twenty-first century: Results from CMIP5. *Geophysical Research Letters* **39**, L17703 (2012).
- 20 Watanabe, M. *et al.* Uncertainty in the ENSO amplitude change from the past to the future. *Geophysical Research Letters* **39**, L20703 (2012).
- 21 Bellenger, H., Guilyardi, E., Leloup, J., Lengaigne, M. & Vialard, J. ENSO representation in climate models: from CMIP3 to CMIP5. *Climate Dynamics* **42**, 1999-2018 (2014).
- 22 Chen, C., Cane, M. A., Wittenberg, A. T. & Chen, D. ENSO in the CMIP5 Simulations: Life Cycles, Diversity, and Responses to Climate Change. *Journal of Climate* **30**, 775-801 (2017).
- 23 Power, S., Delage, F., Chung, C., Kociuba, G. & Keay, K. Robust twenty-first-century projections of El Niño and related precipitation variability. *Nature* **502**, 541-545 (2013).
- 24 Cai, W. *et al.* Increasing frequency of extreme El Niño events due to greenhouse warming. *Nature Climate Change* **4**, 111-116 (2014).
- 25 Yun, K.-S. *et al.* Increasing ENSO–rainfall variability due to changes in future tropical temperature–rainfall relationship. *Communications Earth & Environment* **2**, 43 (2021).
- 26 Timmermann, A. Detecting the Nonstationary Response of ENSO to Greenhouse Warming. *Journal of the Atmospheric Sciences* **56**, 2313-2325 (1999).
- 27 Latif, M. & Keenlyside, N. S. El Niño/Southern Oscillation response to global warming. *Proceedings of the National Academy of Sciences* **106**, 20578-20583 (2009).
- 28 DiNezio, P. N., Vecchi, G. A. & Clement, A. C. Detectability of Changes in the Walker Circulation in Response to Global Warming. *Journal of Climate* **26**, 4038-4048 (2013).
- 29 Bellomo, K. & Clement, A. C. Evidence for weakening of the Walker circulation from cloud observations. *Geophysical Research Letters* **42**, 7758-7766 (2015).
- 30 Chung, E. S. *et al.* Reconciling opposing Walker circulation trends in observations and model projections. *Nature Climate Change* **9**, 405-412 (2019).
- 31 Hamlington, B. D. *et al.* Uncovering an anthropogenic sea-level rise signal in the Pacific Ocean. *Nature Climate Change* **4**, 782-785 (2014).
- 32 Bordbar, M. H., Martin, T., Latif, M. & Park, W. Effects of long-term variability on projections of twenty-first century dynamic sea level. *Nature Climate Change* **5**, 343-347 (2015).
- 33 Timmermann, A., McGregor, S. & Jin, F. F. Wind Effects on Past and Future Regional Sea Level Trends in the Southern Indo-Pacific. *Journal of Climate* **23**, 4429-4437 (2010).
- 34 Eyring, V. *et al.* Overview of the Coupled Model Intercomparison Project Phase 6 (CMIP6) experimental design and organization. *Geosci. Model Dev.* **9**, 1937-1958 (2016).
- 35 Heede, U. K. & Fedorov, A. V. Eastern equatorial Pacific warming delayed by aerosols and thermostat response to CO₂ increase. *Nature Climate Change* **11**, 696-703 (2021).

- 36 Vecchi, G. A. *et al.* Weakening of tropical Pacific atmospheric circulation due to anthropogenic forcing. *Nature* **441**, 73-76 (2006).
- 37 Huang, P. Regional response of annual-mean tropical rainfall to global warming. *Atmospheric Science Letters* **15**, 103-109 (2014).
- 38 McGregor, S. *et al.* Recent Walker circulation strengthening and Pacific cooling amplified by Atlantic warming. *Nature Climate Change* **4**, 888-892 (2014).
- 39 Coats, S. & Karnauskas, K. B. Are Simulated and Observed Twentieth Century Tropical Pacific Sea Surface Temperature Trends Significant Relative to Internal Variability? *Geophysical Research Letters* **44**, 9928-9937 (2017).
- 40 Seager, R. *et al.* Strengthening tropical Pacific zonal sea surface temperature gradient consistent with rising greenhouse gases. *Nature Climate Change* **9**, 517-522 (2019).
- 41 Watanabe, M., Dufresne, J.-L., Kosaka, Y., Mauritsen, T. & Tatebe, H. Enhanced warming constrained by past trends in equatorial Pacific sea surface temperature gradient. *Nature Climate Change* **11**, 33-37 (2020).
- 42 Zhang, L. *et al.* Indian Ocean Warming Trend Reduces Pacific Warming Response to Anthropogenic Greenhouse Gases: An Interbasin Thermostat Mechanism. *Geophysical Research Letters* **46**, 10882-10890 (2019).
- 43 Liepert, B. G. & Previdi, M. Do Models and Observations Disagree on the Rainfall Response to Global Warming? *Journal of Climate* **22**, 3156-3166 (2009).
- 44 Ropelewski, C. F. & Halpert, M. S. Global and Regional Scale Precipitation Patterns Associated with the El Niño/Southern Oscillation. *Monthly Weather Review* **115**, 1606-1626 (1987).
- 45 Deser, C. & Wallace, J. M. Large-Scale Atmospheric Circulation Features of Warm and Cold Episodes in the Tropical Pacific. *Journal of Climate* **3**, 1254-1281 (1990).
- 46 Ham, Y.-G. & Kug, J.-S. Improvement of ENSO Simulation Based on Intermodel Diversity. *Journal of Climate* **28**, 998-1015 (2015).
- 47 Jiang, W., Huang, P., Huang, G. & Ying, J. Origins of the Excessive Westward Extension of ENSO SST Simulated in CMIP5 and CMIP6 Models. *Journal of Climate* **34**, 2839-2851 (2021).
- 48 Huang, P., Chen, D. & Ying, J. Weakening of the tropical atmospheric circulation response to local sea surface temperature anomalies under global warming. *Journal of Climate* **30**, 8149-8158 (2017).
- 49 Ying, J., Huang, P. & Lian, T. Changes in the sensitivity of tropical rainfall response to local sea surface temperature anomalies under global warming. *International Journal of Climatology* **39**, 5801-5814 (2019).
- 50 Beverley, J. D., Collins, M., Lambert, F. H. & Chadwick, R. Future Changes to El Niño Teleconnections over the North Pacific and North America. *Journal of Climate* **34**, 6191-6205 (2021).
- 51 England, M. H. *et al.* Recent intensification of wind-driven circulation in the Pacific and the ongoing warming hiatus. *Nature Climate Change* **4**, 222-227 (2014).
- 52 Bordbar, M. H. *et al.* Uncertainty in near-term global surface warming linked to tropical Pacific climate variability. *Nature Communications* **10**, 1990 (2019).
- 53 Rayner, N. A. *et al.* Global analyses of sea surface temperature, sea ice, and night

marine air temperature since the late nineteenth century. *Journal of Geophysical Research: Atmospheres* **108**, 4407 (2003).

54 Huang, B. *et al.* Extended Reconstructed Sea Surface Temperature, Version 5 (ERSSTv5): Upgrades, Validations, and Intercomparisons. *Journal of Climate* **30**, 8179-8205 (2017).

55 Hirahara, S., Ishii, M. & Fukuda, Y. Centennial-Scale Sea Surface Temperature Analysis and Its Uncertainty. *Journal of Climate* **27**, 57-75 (2014).

56 Cai, W. *et al.* Butterfly effect and a self-modulating El Niño response to global warming. *Nature* **585**, 68-73 (2020).

57 Hawkins, E. & Sutton, R. Time of emergence of climate signals. *Geophysical Research Letters* **39**, L01702 (2012).

58 Johnson, N. C. & Xie, S.-P. Changes in the sea surface temperature threshold for tropical convection. *Nature Geoscience* **3**, 842-845 (2010).

59 Huang, P., Xie, S.-P., Hu, K., Huang, G. & Huang, R. Patterns of the seasonal response of tropical rainfall to global warming. *Nature Geoscience* **6**, 357-361 (2013).

60 Chou, C., Neelin, J. D., Chen, C.-A. & Tu, J.-Y. Evaluating the “Rich-Get-Richer” Mechanism in Tropical Precipitation Change under Global Warming. *Journal of Climate* **22**, 1982-2005 (2009).

61 Ashok, K., Behera, S. K., Rao, S. A., Weng, H. & Yamagata, T. El Niño Modoki and its possible teleconnection. *Journal of Geophysical Research: Oceans* **112** (2007).

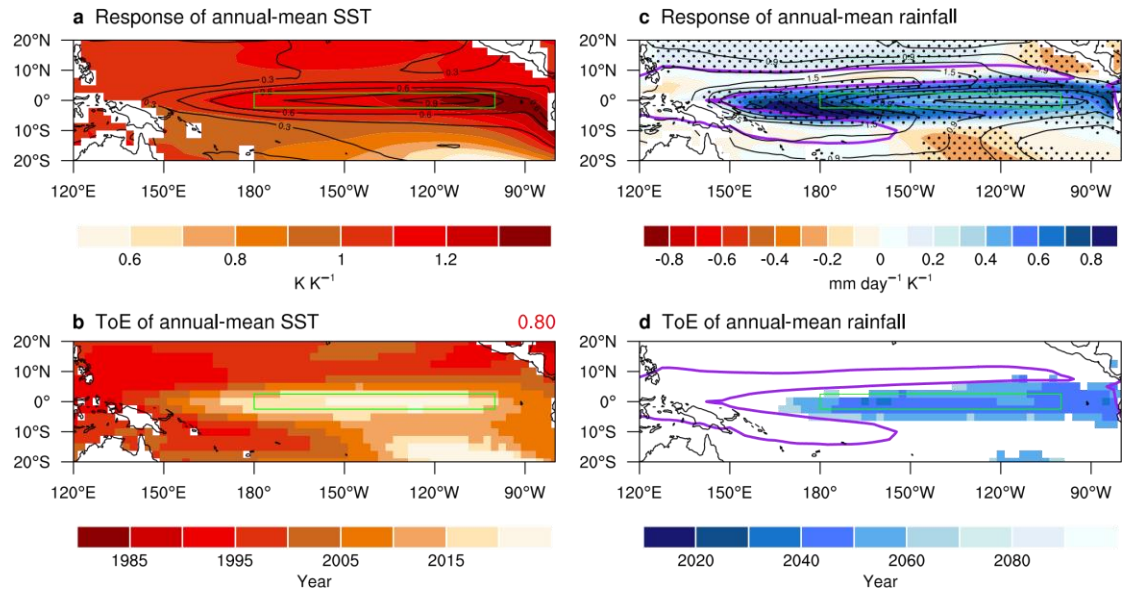


Fig. 1 | Multi-model Ensemble Mean (MEM) response and time of emergence (ToE) of annual-mean SST and rainfall. Figures are computed from models under historical forcing and the SSP585 emission scenario. **a**, Response of annual-mean SST to global warming (see “[Signal and noise of annual-mean SST and rainfall](#)” in [Methods](#)); **b**, ToE of annual-mean SST signal; **c** and **d**, The same as **a** and **b** but for annual-mean rainfall. Contours in **a** and **c** denote the MEM noise of SST (units: K, with an interval of 0.15 K) and rainfall (units: mm day⁻¹, with an interval of 0.3 mm day⁻¹), respectively. The red digit on the upper-right corner of **b** denotes the spatial correlation between MEM ToE signal and MEM noise of SST. Stippling in **c** denotes that more than 70% of models have the same sign. The shaded regions in **b** and **d** denote that more than 70% of models have emergent signals by the year 2099 and are plotted by averaging all the models that show the local ToE by 2099. Purple curves in **c** and **d** denote the 7 mm day⁻¹ contour of rainfall climatology in the reference period. The green box in each plot denotes the eastern equatorial Pacific (2.5°S–2.5°N, 180°W–100°W) region. The MEM increasing signal of annual-mean SST emerges across the whole tropical Pacific, with

694 the latest ToE in the EEP, while that of annual-mean rainfall, which mostly appears in
695 the equatorial Pacific, emerges later.

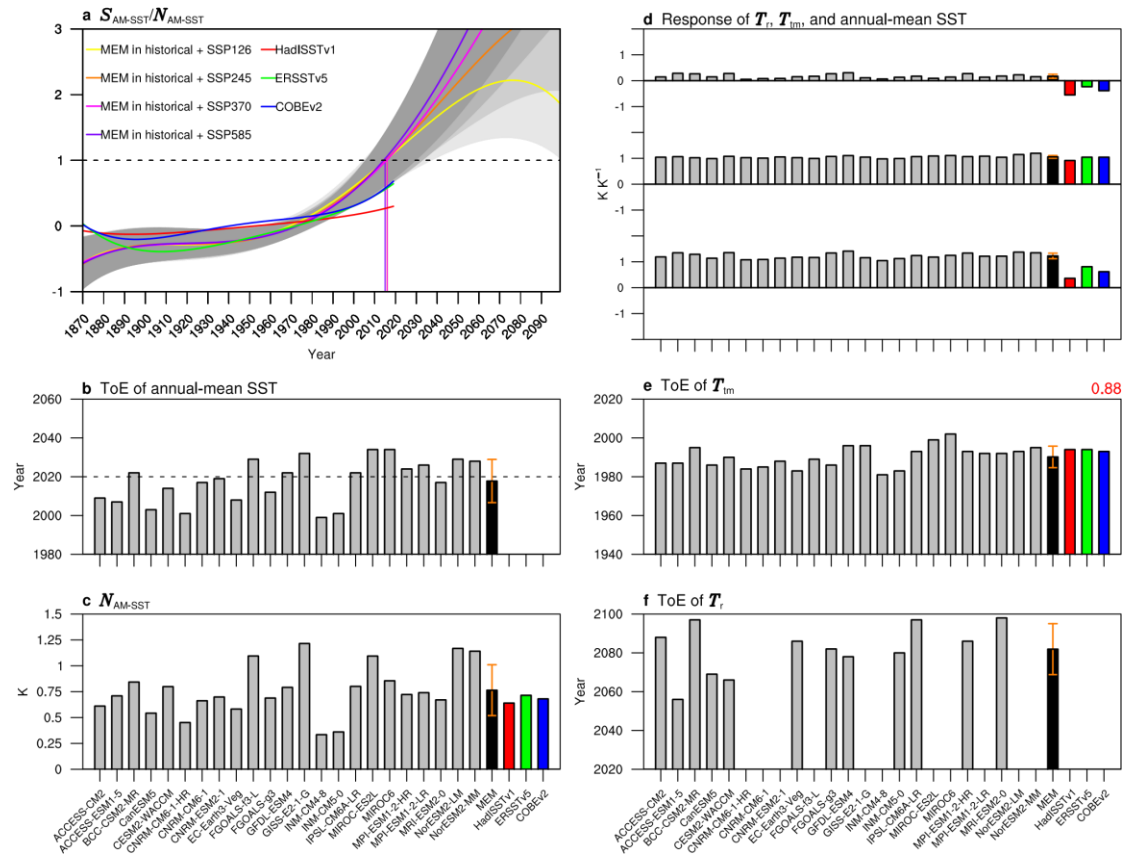


Fig. 2 | ToE of annual-mean SST in the eastern equatorial Pacific. **a**, Signal-to-noise ratio of annual-mean SST in the MEM under historical and four future SSP scenarios and in three observational datasets. The gray shading denotes one inter-model standard deviation, with darker colors indicating a higher emission scenario. The vertical solid lines denote the year when the signal-to-noise ratio exceeds 1.0 in different SSP scenarios; **b** and **c**, ToE (**b**), and noise (**c**) of annual-mean SST (N_{AM-SST}). The horizontal dashed lines in **b** denotes year 2020; **d**, Responses (from top to bottom) of relative SST (T_r), tropical-mean SST (T_{tm}) and annual-mean SST to global warming (units: $K K^{-1}$); **e** and **f**, The same as **b**, but for T_{tm} (**e**), and T_r (**f**). Missing bars in **b** and **f** denote non-emergence in these models (observations) during 1870–2099 (1870–2019), and the MEM results in **b** and **f** are based on non-missing values. The orange error bars denote one inter-model standard deviation. The modelled shown in **b** and **d**–

f are based on historical forcing and the SSP585 emission scenario. The red digit on the upper-right corner of e denotes the inter-model correlation between ToE of annual-mean SST and T_{tm} , which is significant at the 99% confidence level, based on the Student's t test. The detectable signal of annual-mean SST in the EEP mainly reflects the detectable signal of tropical-mean SST, and the model-observation discrepancy in the ToE of annual-mean SST is caused by the different responses between an observed enhancement and a modelled weakening in the west-minus-east SST gradient.

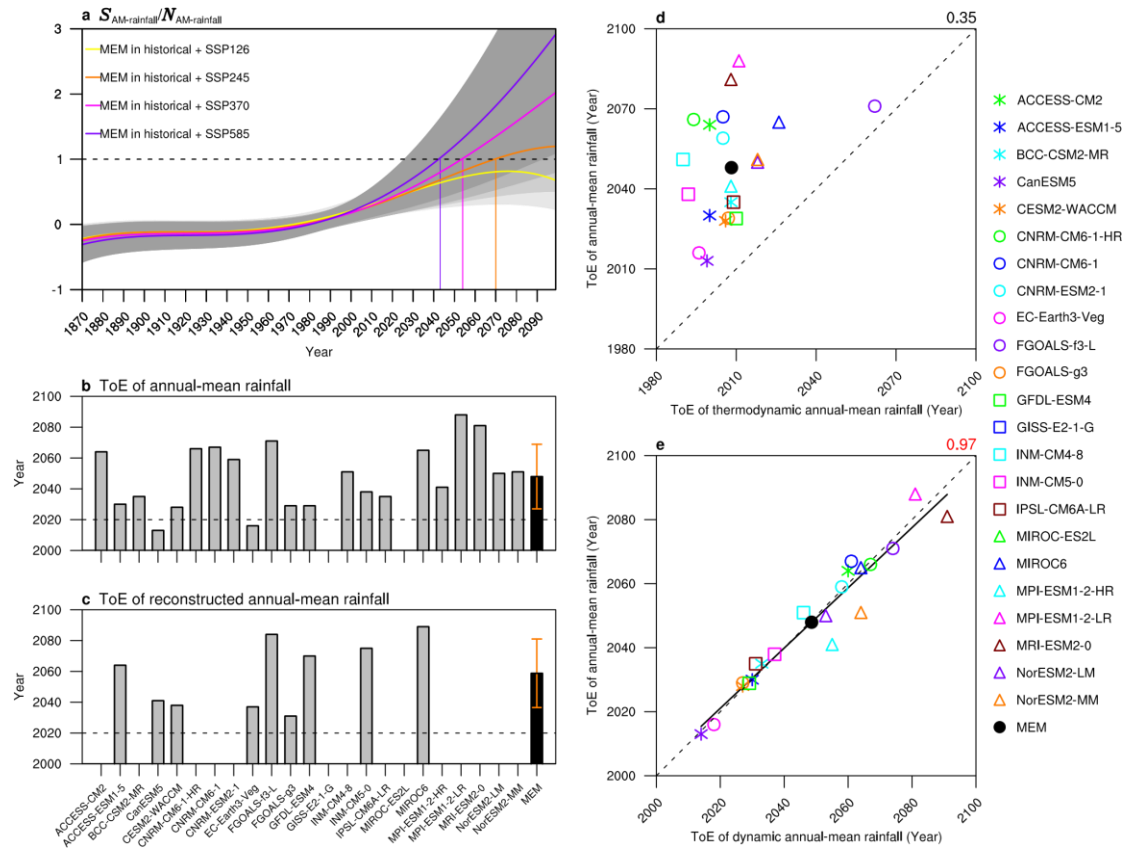


Fig. 3 | ToE of annual-mean rainfall in the eastern equatorial Pacific. a, Signal-to-noise ratio of annual-mean rainfall in the MEM under historical and four future SSP scenarios. The shading denotes one inter-model standard deviation, with darker colors indicating a higher emission scenario. The vertical solid lines denote the year when the signal-to-noise ratio exceeds 1.0 in different SSP scenarios; **b** and **c**, ToE of annual-mean rainfall (**b**) and reconstructed annual-mean rainfall (**c**) (see “[Decomposition of annual-mean SST and rainfall change](#)” in [Methods](#)). The orange error bars denote one inter-model standard deviation; **d** and **e**, Inter-model scatterplots between the ToE for annual-mean rainfall and that for dynamic component (**d**), and thermodynamic component (**e**) of annual-mean rainfall. The black (red) digit on the upper-right corner of **d** (**e**) denotes that the inter-model correlation is insignificant (significant) at the 99% confidence level, based on the Student’s *t* test. The solid line in **e** denotes the inter-

729 model linear regression. Missing bars in **c** and markers in **e** denote non-emergence
730 during 1870–2099, and the MEM result is based on non-missing values. Shown in **b–e**
731 is based on models under historical forcing and the SSP585 emission scenario. The later
732 ToE of annual-mean rainfall than that of annual-mean SST, which appears in around
733 mid-century based on the MEM, is sensitive to emission scenario and is determined by
734 the ToE of the dynamic component.

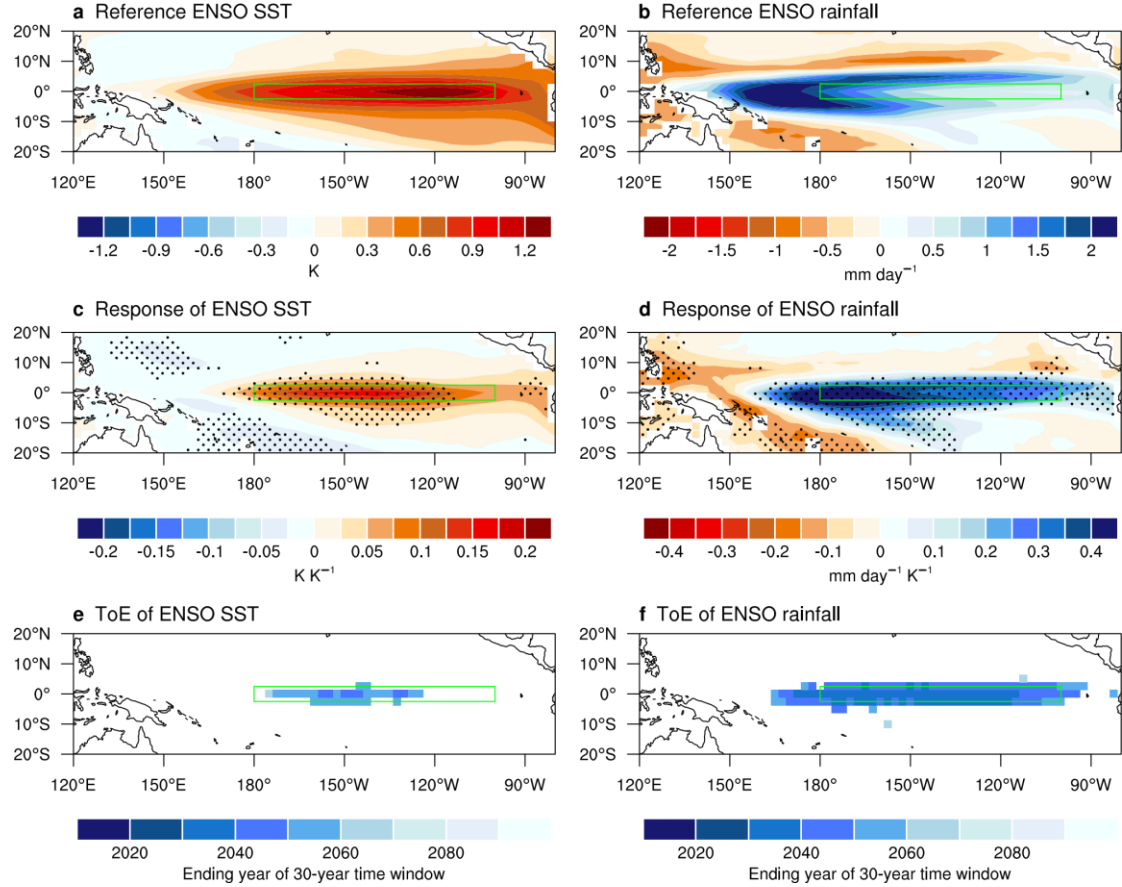
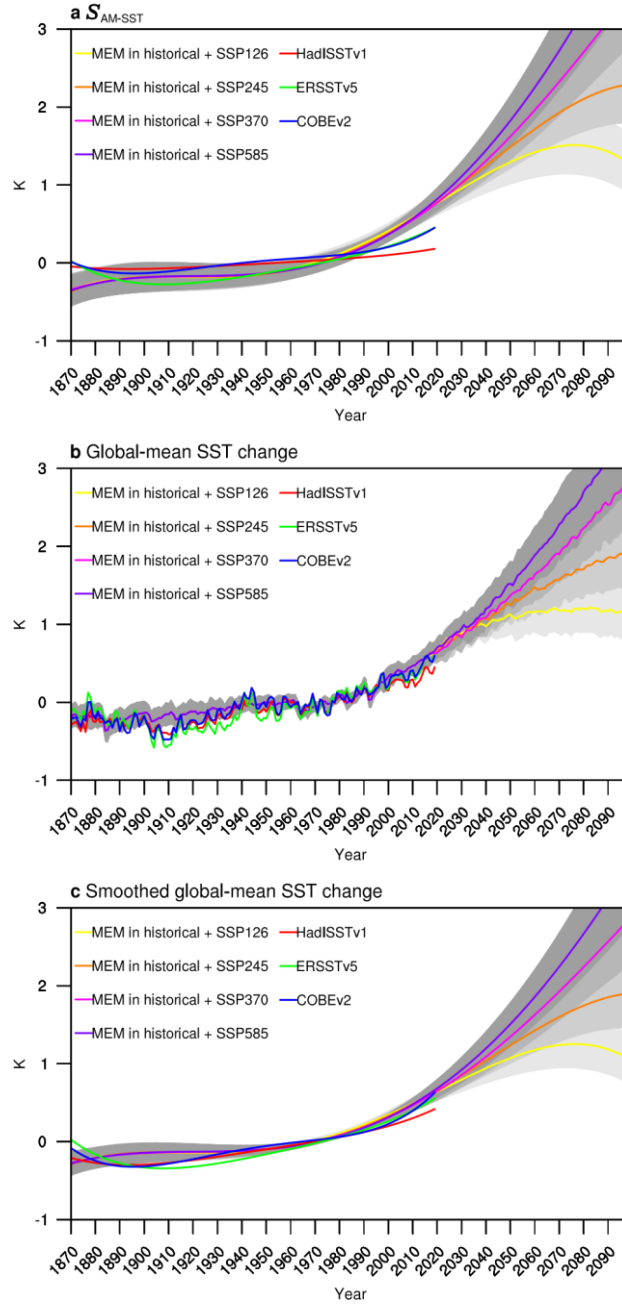
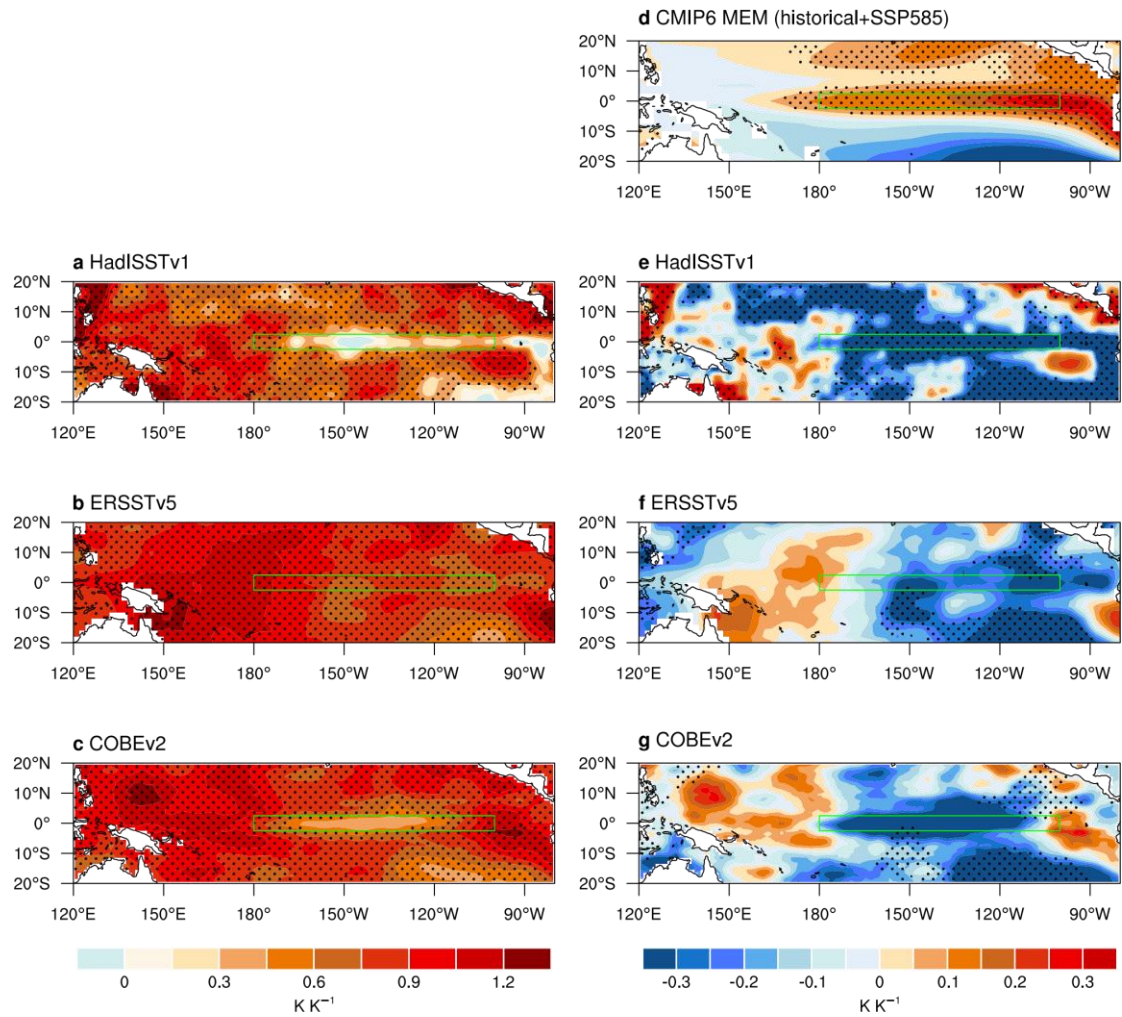


Fig. 4 | MEM response and ToE of ENSO SST and rainfall. **a–b**, Spatial patterns of ENSO SST (**a**) and rainfall (**b**) in the reference period (see “[ENSO-related SST and rainfall variability](#)” in [Methods](#)); **c** and **d**, Responses of ENSO SST (**c**) and rainfall (**d**) to global warming, which are calculated by regressing the signal of ENSO SST and rainfall onto global warming time series of $\tilde{T}_c(t_e)$, respectively. Stippling denotes where more than 70% of models have the same sign; **e** and **f**, ToE of ENSO SST (**e**) and rainfall (**f**). The shaded regions denote that more than 70% of models have emergent signals, and are plotted by averaging all the models that show the local ToE. Panels in **c–f** are based on models under historical forcing and the SSP585 emission scenario. Increasing signals of ENSO SST and rainfall with time, both of which involve not only amplitude change but also pattern shifts, have yet been detected.

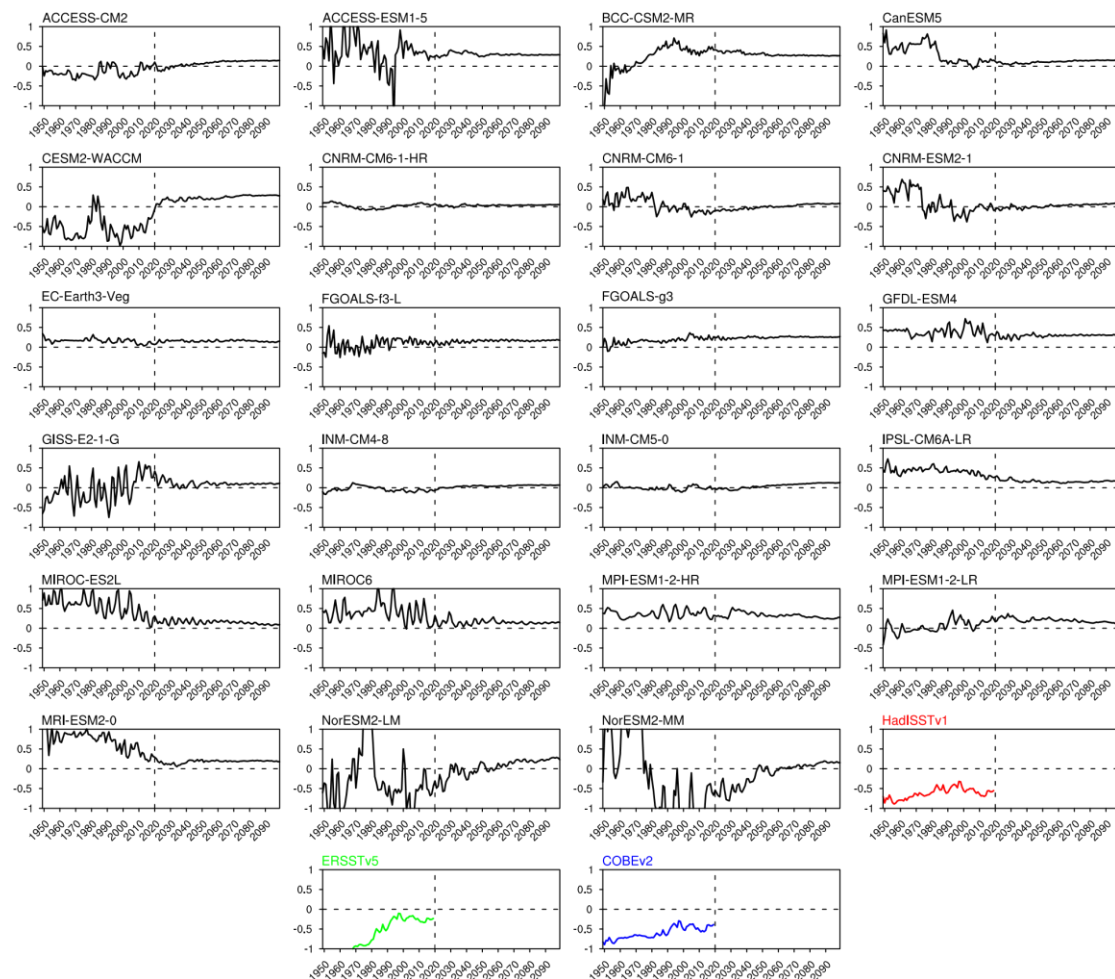
year time window when the MEM signal of ENSO SST exceeds the defined threshold value; **b**, The same as **a**, but for ENSO rainfall only in the MEM. The MEM threshold value for estimating the MEM detectable signal of ENSO rainfall is 0.18 (horizontal dashed line in **b**); **c**, ToE of ENSO SST under historical forcing and the SSP585 emission scenario; missing bars denote that signals do not emergence before 2099 (2019) for these models (observations). The orange error bars denote one inter-model standard deviation; **d**, The same as **c**, but for ENSO rainfall. **e–g**, Inter-model scatterplots between the ToE of ENSO rainfall and that of dynamic component (**e**), and thermodynamic component (**f**) of ENSO rainfall, and between the ToE of dynamic component of ENSO rainfall and that of 30-year climatological relative SST (**g**). The black (red) digit on the upper-right corner of **e–g** denotes that the inter-model correlation is insignificant (significant) at the 99% confidence level, based on the Student's *t* test. The solid lines in **f** and **g** denote the inter-model linear regressions. The modelled ToE of ENSO rainfall, which is dominated by the ToE of its dynamical component, is projected to emerge by around 2040 based on the MEM regardless of emission scenarios, around 30 years earlier than that of ENSO SST, which is with some sensitivity to emission scenarios.



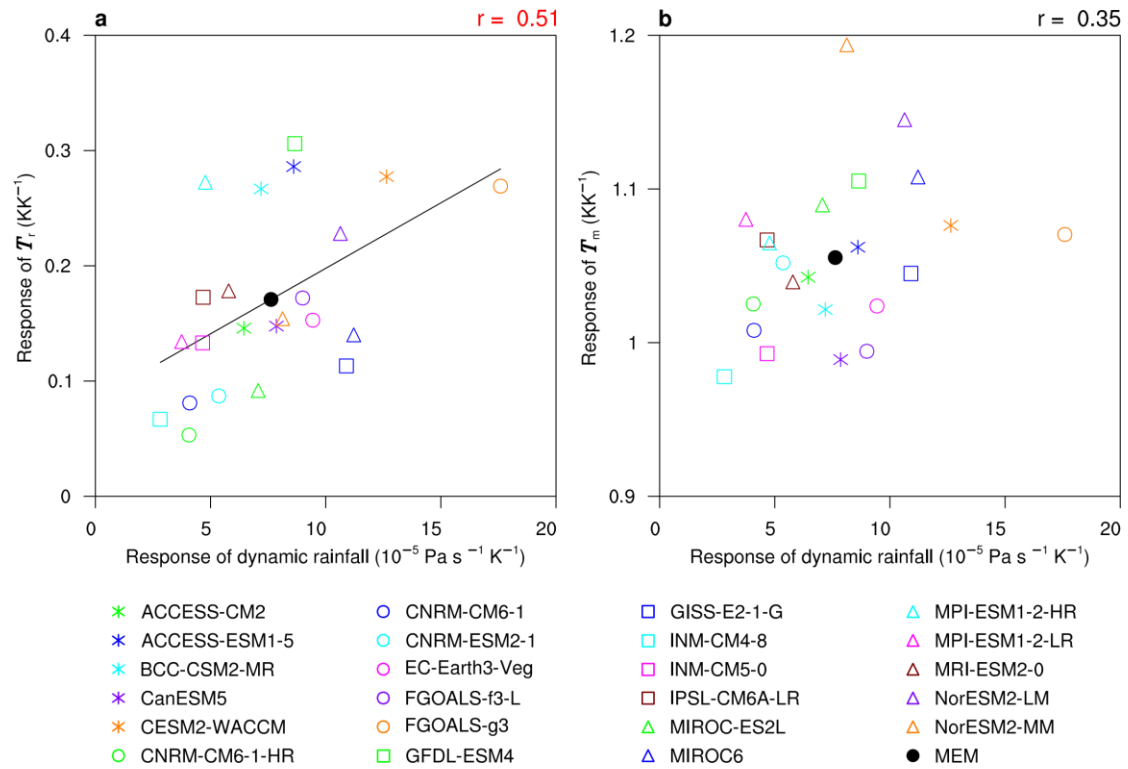
Extended Data Fig. 1 | Signal of annual-mean SST and global mean (60S-60N) SST change. **a**, Signal of annual-mean SST in the EEP in MEM under historical and four future forcing scenarios and in observations. The shading denotes one inter-model standard deviation, with darker colors indicating higher emission scenarios; **b** and **c**, The same as **a**, but for global-mean SST change (**b**), and smoothed global-mean SST change by fitting a fourth order polynomial (**c**).



Extended Data Fig. 2 | Response of annual-mean SST to global warming. a–c,
 Response of annual-mean SST to global warming for HadISSTv1, ERSSTv5 and
 COBEv2, respectively; **d**, MEM response of relative SST to global warming under
 historical and the SSP585 scenario; **e–g**, The same as **a–c**, but for relative SST. The
 green box in each plot denotes the eastern equatorial Pacific (2.5°S–2.5°N, 180°W–
 100°W). Stippling in **a–c** and **e–g** indicates that the regressions are significant above
 the 95% confidence level based on the Student's *t* test, while stippling in **d** denotes that
 more than 70% of models have the same sign.



Extended Data Fig. 3 | EEP relative SST response to global warming calculated in increasing length of periods. Shown is for response averaged over the EEP (2.5°S–2.5°N, 180°W–100°W) for 23 CMIP6 models under historical and the SSP585 scenario and in observations (y-axis, units: K K⁻¹). The x-axis indicates the ending year of a period for calculation of the response, all starting from 1870; for example, when ending in 1949 (the first year shown), the response is calculated over the period from 1870–1949, and when ending in 2050 the response is calculated over the period from 1870–2050.



Extended Data Fig. 4 | Inter-model relationship between dynamic rainfall

response and annual-mean SST response. a and b, Scatter plots of inter-model

responses of dynamic rainfall with responses of relative SST (a) and tropical-mean SST

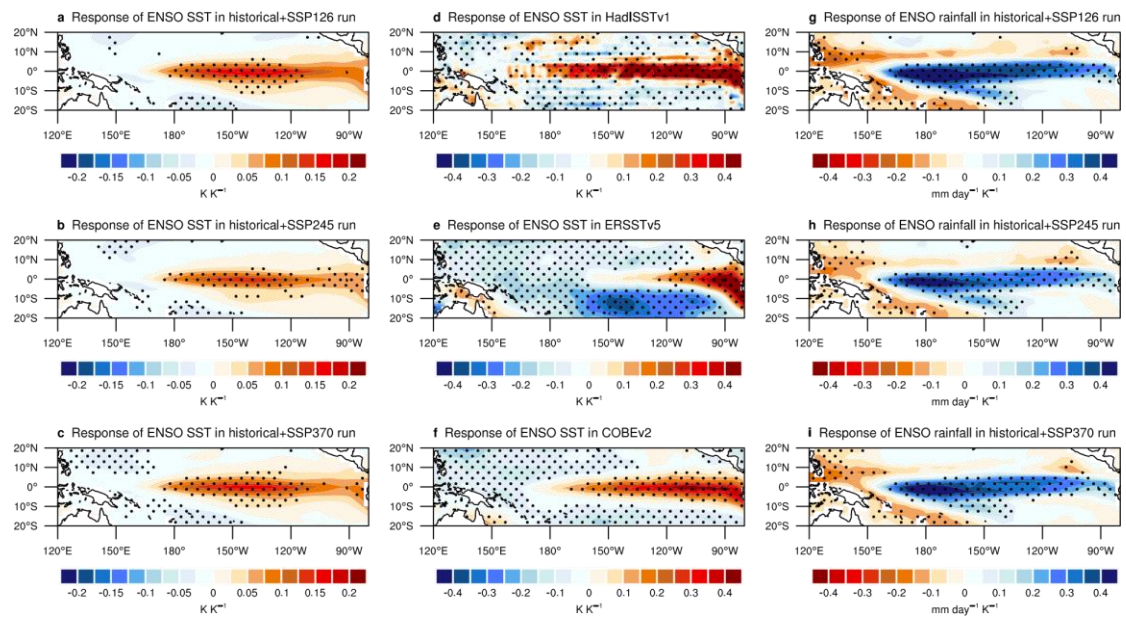
(b) in the EEP under historical and the SSP585 scenario. The solid line in a denotes the

linear regression. Digits on the upper-right corner of each plot are the inter-model

correlations, with red (black) indicating statistically significant (insignificant) at the 95%

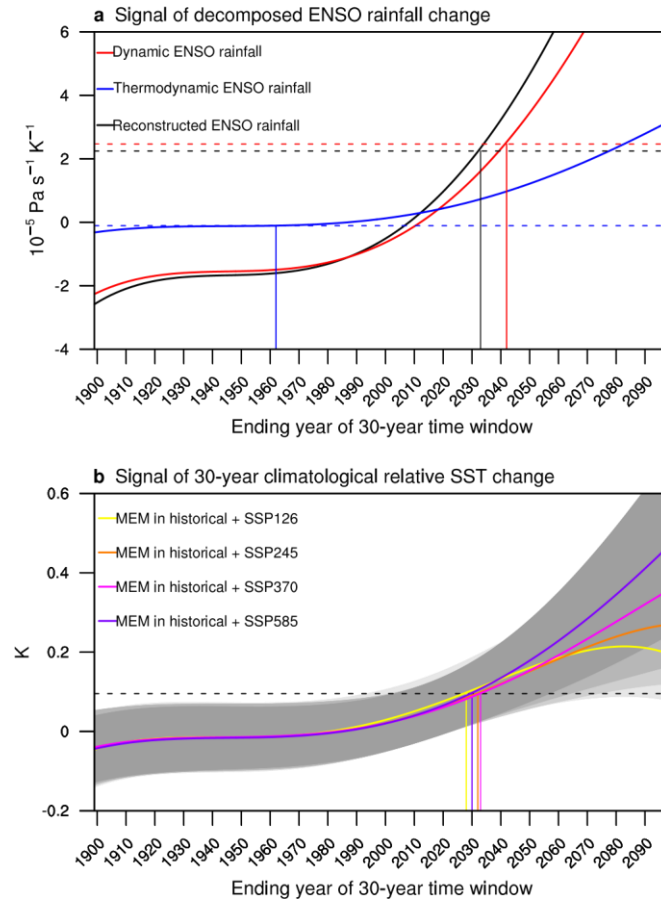
confidence level, based on the Student's t test. No regression line is plotted in (b) as the

correlation is not significant.



Extended Data Fig. 5 | Responses of ENSO SST and rainfall to global warming.

a–c, MEM Responses of ENSO SST under historical and the SSP126 (**a**), SSP245 (**b**), and SSP370 (**c**) scenarios. **d–f**, The same as **a–c**, but for HadISSTv1 (**d**), ERSSTv5 (**e**) and COBEv2 (**f**), respectively. **g–i**, The same as **a–c**, but for ENSO rainfall. Stippling in **a–c** and **g–i** denotes that more than 70% of models have the same sign, while in **d–f** indicates that the regressions are significant above the 95% confidence level based on the Student's t test.



Extended Data Fig. 6 | Signal of decomposed ENSO rainfall and 30-year climatological-mean relative SST change. **a**, Signal of dynamic (red curve), thermodynamic (blue curve), and reconstructed (black curve) ENSO rainfall in the EEP in MEM under historical and SSP585 scenario. The horizontal dashed lines denote the MEM threshold value for estimating the MEM detectable signal of dynamic (red), thermodynamic (blue), and reconstructed (black) ENSO rainfall. The vertical solid lines denote the ending year of a 30-year time window when the MEM signal of dynamic (red), thermodynamic (blue), and reconstructed (black) ENSO rainfall exceeds the defined threshold value. **b**, The same as Fig. 5b, but for the 30-year climatological relative SST change (see “[Decomposition of 30-year climatological SST and ENSO rainfall change](#)” in [Methods](#)).

